



Synthesis and Study on Photogenerated Charge Behavior of Novel Pt/CeO₂/ZnO Ternary Composites with Enhanced Photocatalytic Degradation Activity

Peng Zhao¹ · Jinteng Zhang¹ · Jingjing Jiang¹ · Hongtao Wang¹ · Tengfeng Xie¹ · Yanhong Lin¹

Received: 26 June 2019 / Accepted: 3 September 2019 / Published online: 14 September 2019
© Springer Science+Business Media, LLC, part of Springer Nature 2019

Abstract

A novel Pt/CeO₂/ZnO ternary composite is synthesized via two simple procedures of hydrothermal and photoreduction. The crystal structure, morphology, and composition of as-prepared samples are characterized by XRD, SEM, HRTEM, XPS and UV–Vis DRS. Because both ZnO and CeO₂ are good photocatalytic semiconductors, photocatalytic activities of the samples are evaluated by the degradation of phenol aqueous solution (25 mg/L). Under the strong interaction among the Pt, CeO₂ and ZnO, the maximum photocatalytic activity is observed in the Pt/CeO₂/ZnO ternary composites and 91% phenol can be degraded in 60 min under UV light irradiation. The probable photocatalytic mechanism is discussed by active species trapping experiments along with SPV, TPV, PL and PA measurements. The enhanced photocatalytic activity is attributed to the redox cycle of Ce⁴⁺ ↔ Ce³⁺, the effective interface between ZnO and CeO₂ as well as the electron transfer action of Pt nanoparticles. The photocatalytic activity almost unchanged after four cycles and proves excellent reusable photocatalysts. This work shows the synergistic effect of rare earth elements and noble metals in the photocatalytic process, which facilitates their practical application in toxic pollution abatement.

Keywords Ternary composites · Rare elements · Photocatalytic mechanism · TPV · Pollution abatement

1 Introduction

In recent years, due to the accelerating procession of industrialization, water-pollution poses a great threat to environmental system and human health. It is absolutely essential to find a way to solve this problem [1]. There are many traditional methods used in the field of water treatment, such as coagulation, precipitation, ion exchange, membrane separation and adsorption etc. However, the disadvantages of high consumption, high operational cost, low selectivity and the generation of severe secondary pollution also limit their application [2]. Almost 30 years after its discovery, photocatalysis is becoming one of the most promising “green” chemistry technologies on address environmental and energy emergencies [3]. Up to now, plenty of papers about the synthesis and application photocatalytic materials such as ZnO

[4–7], TiO₂ [8–10], Bi₂O₃ [11], C₃N₄ [12–14], Ag₃PO₄ [15] have been reported. Among them, ZnO, a typical II–VI groups semiconductor material, has receives more attention owing to its large exciton binding energy (~60 meV), high chemical stability, facile preparation method, cost effectiveness, controlled morphologies, eco-friendly and non-toxic [16]. Nevertheless, low quantum efficiency, narrow spectral absorption range and serious carriers recombination rate are significant drawbacks which restrict its further applications. To enhance the photocatalytic performance of ZnO, many researchers have modified ZnO with various strategies, such as ion doping, noble metal loading [17], surface oxygen deficiency modification [18] and hybridizing ZnO with other materials. In particular, fabricating heterojunction structures has aroused great interest [19] because high efficiency of the interfacial charge transfer can reduce the recombination of photogenerated carriers and increase carriers lifetime. CeO₂ is chosen as a well coupled semiconductor because of its similar band gap energy and matched band gap structure with ZnO. Besides, CeO₂ is a typical active catalyst with superior oxidation performance due to its Ce⁴⁺ ↔ Ce³⁺ redox cycle, the different electronic structures of

✉ Yanhong Lin
linyh@jlu.edu.cn

¹ College of Chemistry, Jilin University, Changchun 130012, People's Republic of China

Ce^{3+} with $4f^1 5d^0$ and Ce^{4+} with $4f^0 5d^0$ atomic orbital will lead to different photochemistry properties [20]. Therefore, some researchers have combined the two semiconductors to design highly performance oxidation catalyst. Wang and coworkers synthesized CeO_2/ZnO heterostructures through a facile solid-state reaction method, and the photocatalytic rate of CeO_2/ZnO heterojunctions is 4.6 times higher than that of pure ZnO [21]. Lamba et al. successfully prepared CeO_2/ZnO materials, the results reveal that the composite exhibits high photocatalytic removal efficiency of blue 15 dye under solar light [22]. In these reports, it has been proved that construct CeO_2/ZnO heterojunction can enhance the separation efficiency of photogenerated carriers and extend carriers lifetime.

As is known to all, the photocatalytic process usually included three steps: (1) absorbing photons with energy larger than bandgap energy of photocatalyst and excites electrons from the VB to the CB, (2) the separation and migration of photogenerated charge carriers to the surface of the semiconductor, (3) the redox reactions occurring on the photocatalyst surface. Among them, the migration of photogenerated charge carriers is the key process which takes place in femtosecond time. If the photogenerated charge carriers can be transferred in time, the photocatalytic activity will be further improved. Noble metal modification is recognized as an ideal approach, Pt plays an important role in determining the carriers separation and transfer efficiency across interface between metal and semiconductors. By coupling with TiO_2 [23], CdS [24], Bi_2WO_6 [25], Fe_2O_3 [26], Pt can serve as the electron acceptor and provide a fast transmission path for the photogenerated charges at the semiconductor interface [27], which have a positive effect on the quantum yield and the photocatalytic activity of photocatalyst. However, few research papers about Pt/heterojunction or Pt/homojunction have been reported. To make better use of the synergistic effect among the multivariant hybrid nanomaterials, it is important to understand the influences of materials on the behavior of photogenerated carriers across the metal/semiconductor and semiconductor/semiconductor. CeO_2/ZnO photocatalyst based on the different nanostructure have been studied intensively, more attentions have not been paid on the Pt modified CeO_2/ZnO ternary composites up to now. Hence, it is necessary to study the performance and mechanism of the Pt/ CeO_2/ZnO ternary composites.

Here, the prepared and characterization of the novel Pt/ CeO_2/ZnO ternary composites is presented, and the synergistic effect has been also studied. Its degradation result shows that the removal efficiency of phenol is able to achieve 91% after 60 min UV light irradiation, which is superior to pure ZnO, CeO_2 as well as CeO_2/ZnO composites. Based on the results of PL, SPV and TPV experiments, the superior catalytic performance can be ascribed to the n–n heterojunction between ZnO and CeO_2 , the redox cycle of $\text{Ce}^{4+} \leftrightarrow$

Ce^{3+} , and the fast electronics transmission path provided by Pt nanoparticles. A mechanism for the enhancement of the photocatalytic performances is also proposed.

2 Experimental

2.1 Materials

All the reagents used in our experiment were analytical grade and without further purification. Zinc acetate dehydrate [$\text{Zn}(\text{CH}_3\text{COO})_2 \cdot 2\text{H}_2\text{O}$, Xilong Chemical Co., Ltd, $\geq 99.0\%$], sodium hydroxide (NaOH, Beijing Chemical Works, $\geq 96.0\%$), Cerium nitrate [$\text{Ce}(\text{NO}_3)_3 \cdot 6\text{H}_2\text{O}$, Aladdin reagent, $\geq 99.5\%$], hexachloroplatinic acid ($\text{H}_2\text{PtCl}_6 \cdot 6\text{H}_2\text{O}$, Sinopharm Chemical Reagent Co., $\geq 37\%$), ethanol ($\text{C}_2\text{H}_5\text{OH}$) and Deionized (DI) water.

2.2 Preparation of ZnO Nanoflowers and CeO_2/ZnO Composites

ZnO nanoflowers were synthesized according to our previous report [28]. In a typical procedure, 4 mmol $\text{Zn}(\text{CH}_3\text{COO})_2 \cdot 2\text{H}_2\text{O}$ were dissolved in 60 mL DI water, then 20 mL of 3 M NaOH aqueous solution were introduced into the above solution with stirring constantly. When the mixture solution became transparent, the solutions were transferred into a 100 mL Teflon stainless-steel autoclave, sealed and hydrothermally treated in a oven at 150°C for 10 h. When the reactions were completed, the reaction system was cooled to ambient temperature. The white solid was obtained by centrifugation and washed with DI water and absolute ethanol three times, respectively. Finally, the powders were put into an alumina crucible, calcined at 600°C ($2^\circ\text{C}/\text{min}$) for 2.5 h.

A series of CeO_2/ZnO composites were synthesized by added x mol percent ($x=0.5, 1, 3, 5$) of $\text{Ce}(\text{NO}_3)_3 \cdot 6\text{H}_2\text{O}$ to $\text{Zn}(\text{CH}_3\text{COO})_2$ solution, and other steps were consistent with the synthesis of ZnO nanoflowers. For comparison, the pure CeO_2 materials were also prepared by the same method but without the addition of $\text{Zn}(\text{CH}_3\text{COO})_2$.

2.3 Preparation of Pt/ CeO_2/ZnO Ternary Composites

In this step, we chose the 3% CeO_2/ZnO composites as precursor, and deposited Pt on its surface with the assistance of UV light. Briefly, 0.163 g CeO_2/ZnO composites was dispersed in 50 mL water/ethanol (1/1, v/v) solutions, ultrasonicated for 10 min to obtain a homogeneously dispersed suspension, then 1 mL H_2PtCl_6 solution (19 mmol/L) was dropped into the above mixture solution. At the same time, N_2 gas was bubbled into the mixture with vigorously stirred for 0.5 h to remove dissolved O_2 . The suspension was then

illuminated with KI UV lamp (60 mW/cm^2) for 1 h. Finally, the products were centrifuged, washed several times with DI water and ethanol, dried in a vacuum oven at $60 \text{ }^\circ\text{C}$ for 12 h. The obtained sample was labeled as Pt/CeO₂/ZnO.

2.4 Characterization

The crystal phase of prepared samples were characterized by power X-ray diffraction (XRD) with a Rigaku D/Max-2550 diffractometer using Cu K α 1 radiation in the 2θ range of 20° – 80° . The morphology of samples was studied by scanning electron microscopy (SEM) (shimadzu, ss-550). Nano-size and lattice fringes were recorded by high resolution transmission electron microscopy (HRTEM) images using the TECNAIG2 (FEI company) worked at 200 kV. X-ray photoelectron spectroscopy (XPS) measurements were carried out on a Thermo VG Scientific ESCALAB 250 spectrometer using monochromatized Al K α excitation. UV–Visible diffuse reflectance spectra (UV–Vis DRS) were obtained by a Shimadzu UV-3600 spectrophotometer. Surface photovoltage (SPV) system was used to measure photogenerated carriers separation efficiency, it was consisted of monochromatic light, a lock-in amplifier (SR830-DSP) with a light chopper (SR540). Transient photovoltage (TPV) for the detection of photogenerated charge behavior at specific wavelengths which included a laser radiation pulse (wavelength of 355 nm and pulse width of 5 ns) from the third-harmonic Nd: YAG laser (Polaris II, New Wave Research, Inc) and a 500 MHz digital phosphor oscilloscope (TDS 5054, Tektronix). Photoluminescence (PL) spectra with an excitation wavelength of 325 nm were measured on a FLUORO-MAX-4. The photoacoustic (PA) signals were accomplished as SPV measurement with a current-to-voltage converter.

2.5 Photocatalytic experiments

The photodegradation experiments were performed in a cylindrical Pyrex flask with quartz windows (50 mL). In a typical photocatalytic activity test, 20 mg prepared samples were dispersed in 20 mL phenol solution (25 mg/L). The mixtures were sonicated for 5 min, and then maintained in darkness with constantly magnetic stirring for 30 min to established adsorption–desorption equilibrium. Afterwards, the suspension was irradiated with the KI UV lamp (30 mW/cm^2), every 10 min, 800 μL of the suspension was taken from the degrading pool. Before measurement, the solution was centrifuged with the speed of 12,000 rpm to remove photocatalyst particles. The concentration of phenol was determined by measuring the maximum absorption peak (phenolic hydroxyl group) at 269 nm through the UV–Vis spectrophotometer (UV-3600). According to Lambert–Beer law $A = \epsilon bc$, absorbance and concentration shows good linear relation. So we can use the absorbance intensity

reasonably to substitute the concentration. The formula for the calculation of the degradation rate is given below:

$$\text{Photodegradation (\%)} = \frac{C_0 - C}{C_0} \times 100 \quad (1)$$

where C_0 is the initial concentration of phenol when achieved adsorption/desorption equilibrium in dark ($t=0$), and C is the concentration of phenol at time t (min).

3 Result and Discussion

3.1 XRD Characterization

The XRD patterns of the different samples are shown in Fig. 1. It can be seen from Fig. 1a, all of the diffraction peaks are well indexed with the standard card of wurtzite ZnO

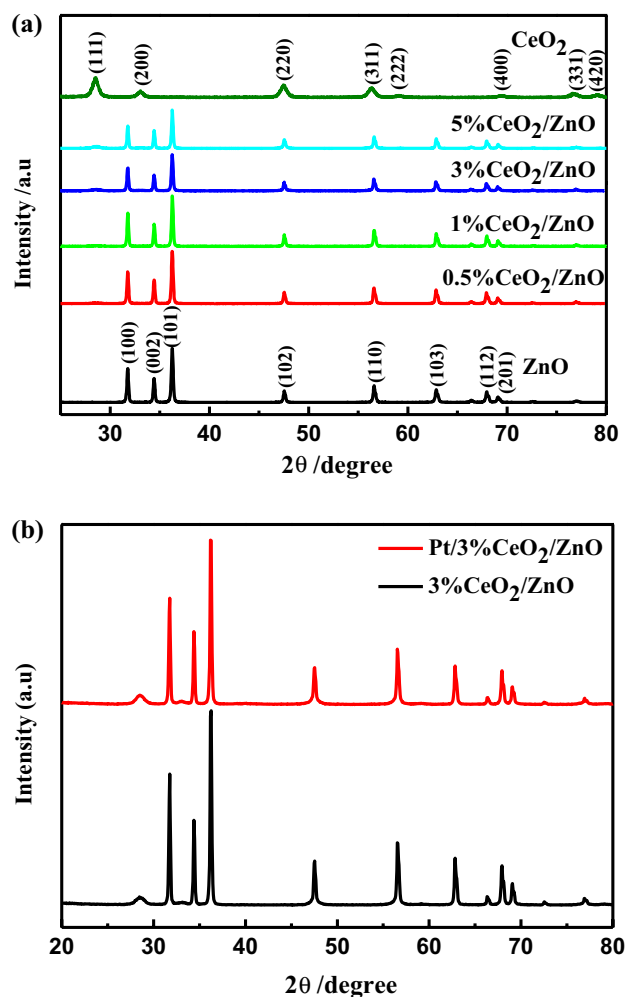


Fig. 1 XRD patterns for pure ZnO, CeO₂/ZnO and Pt/3%CeO₂/ZnO composites

(JPCDS#36-1451) and cubic CeO_2 (JCPDS No. 81-0792). There are no extra peaks observed, indicating no impurities present in as-prepared CeO_2/ZnO composites. With the increasing of CeO_2 content in ZnO, the peak intensities belonging to ZnO gradually weaken, a weak peak of (111) lattice plane of CeO_2 can be observed around 28° in the XRD patterns. However, as shown in Fig. 1b, the diffraction peaks of Pt are too weak to be observed in the Pt/ CeO_2/ZnO ternary hybrid composites, which is attributed to the small amount and high dispersion of Pt nanoparticles.

3.2 FESEM and TEM Characterization

The morphological and size information were characterized by FESEM and TEM. Figure 2a shows the typical FESEM image of the ZnO nanoflowers, the samples are self-assembled from nanorods with the lengths of 3–3.5 μm and diameters about 400 nm. In Fig. 2b, after coupled with CeO_2 and Pt, owing to a lot of CeO_2 and Pt particles have been well attached on the ZnO surface, the surface of ZnO nanorods become coarse.

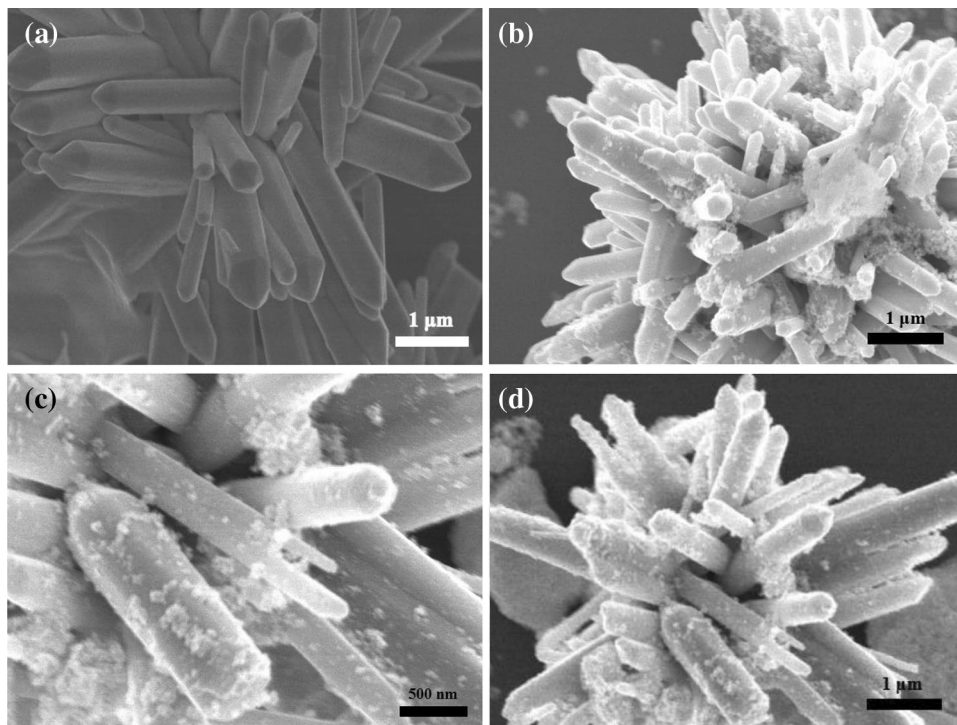
TEM image of Pt/ CeO_2/ZnO is presented in Fig. 3, the TEM images are consistent with the FESEM ones. Many uniform dark spots below 10 nm in size are distributed on the surface of ZnO nanorods. The HRTEM image shows ordered lattice fringes, the lattice fringes with the spacing of 0.314 nm and 0.242 nm are in accord with the (111) plane of CeO_2 and the (101) plane of ZnO, respectively. Unfortunately, we failed to detect the lattice fringes of Pt, which

may be attributed to the highly dispersed of Pt nanoparticles. EDX mapping is used to study the detailed elemental composition and prove the existence of Pt nanoparticles. As shown in Fig. 3d–g, the result indicates Zn, O, Ce, Pt are included in as-prepared Pt/ CeO_2/ZnO sample, CeO_2 and Pt nanoparticles can be well distributed on the surface of ZnO.

3.3 XPS Characterization

To further verify the existence of Pt and obtain valence state information of various elements, the XPS measurement is carried out. The full-scale XPS spectrum of Pt/ CeO_2/ZnO sample shows that its surface includes O, Zn, Ce, Pt elements (Fig. 4a). Figure 4b–f is the high resolution XPS spectra of C 1s, Pt 4f, O 1s, Ce 3d and Zn 2p, respectively. Among them, the C 1s peak at 284.6 eV comes from the adhesive hydrocarbon from the XPS instrument itself (Fig. 4b). The O 1s peak (Fig. 4c) can be fitted into two peaks at 529.36 eV and 531.00 eV. The peak located at 529.36 eV is related to Zn–O bond, and the peak at 531.00 eV is connected with O^{2-} ions in the oxygen deficient regions within the matrix of ZnO [29]. In addition, the binding energies of Zn 2p_{3/2} and Zn 2p_{1/2} (Fig. 4d) are located at 1020.50 eV and 1043.66 eV, respectively. Moreover, the existence of metallic Pt^0 is confirmed by the peaks at 70.95 eV (Pt 4f_{7/2}) and 74.17 eV (Pt 4f_{5/2}) (Fig. 4e). The Ce 3d spectrum can be fitted into six peaks, Ce ions exist in the CeO_2 in two forms of valence states, which is proved by the binding energies of Ce^{4+} 3d_{3/2} (915.49 eV), Ce^{4+} 3d_{5/2} (899.76 eV and 897.03 eV), Ce^{3+}

Fig. 2 FESEM images of **a** pure ZnO, **b** 3% CeO_2/ZnO , **c**, **d** Pt/3% CeO_2/ZnO



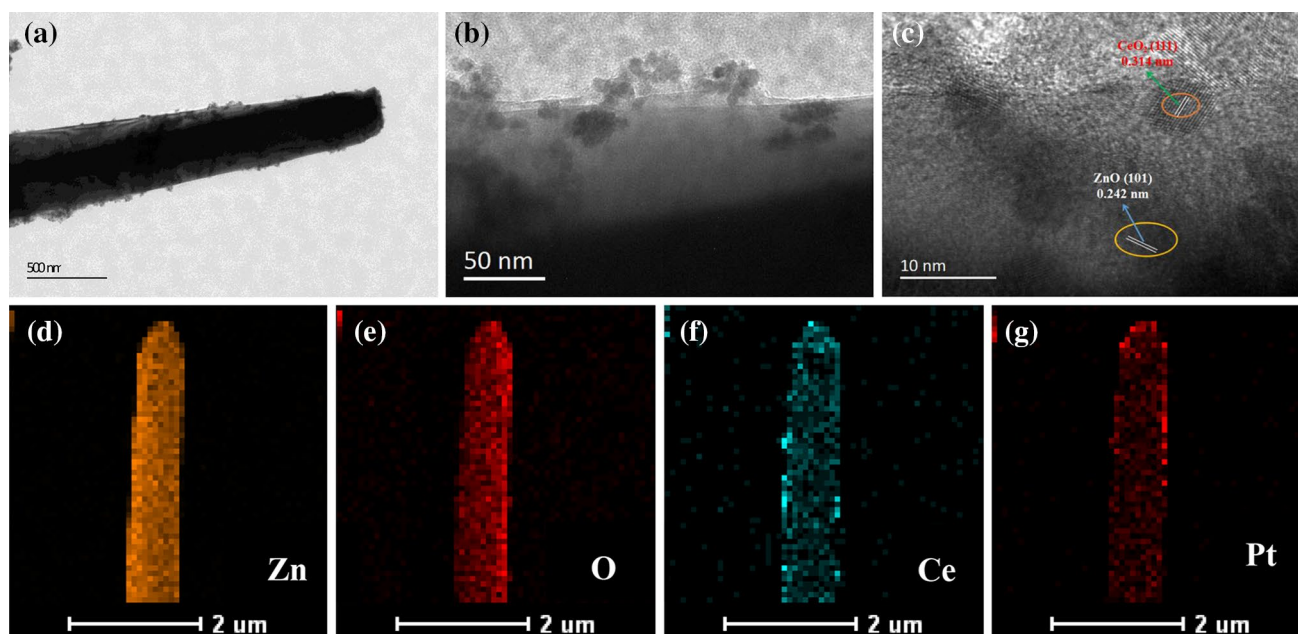


Fig. 3 a, b TEM and c HRTEM pictures of Pt/3%CeO₂/ZnO sample, d–g EDX mapping images of the Pt/3%CeO₂/ZnO sample

3d_{3/2} (906.14 eV), Ce³⁺ 3d_{5/2} (886.95 eV and 880.91 eV) (Fig. 4f) [30]. CeO₂ can form a continuum of oxygen deficient non-stoichiometric oxides under certain conditions, the so-called α phase, with compositions in the range of $0 < y < 0.286$ for CeO_{2-y} [31]. Therefore, Ce³⁺ originating from lattice defect will exist on the surface of the CeO₂ catalysts. The above analysis successfully proves that Pt, CeO₂, ZnO coexisted in the Pt/CeO₂/ZnO composites.

3.4 UV–Vis DRS Characterization

The optical properties of the samples are determined by the UV–vis diffuse reflectance spectra and displayed in Fig. 5. Pure ZnO shows strong UV absorption with the absorption band edge of 420 nm. CeO₂ are quite similar to other reported CeO₂ and exhibits part of absorption in visible light region [32], which can be attributed to large numbers of surface defect states in the as-prepared CeO₂. With the increase of CeO₂ contents, the enhanced absorption are observed for the presence of CeO₂ nanoparticles and the incorporation of Ce⁴⁺ ions into the ZnO lattice sites. As direct band gap semiconductor, the band gap energy can be calculated by Tauc approach [33]:

$$\alpha = \frac{c(h\nu - E_g^{\text{bulk}})^2}{h\nu} \quad (2)$$

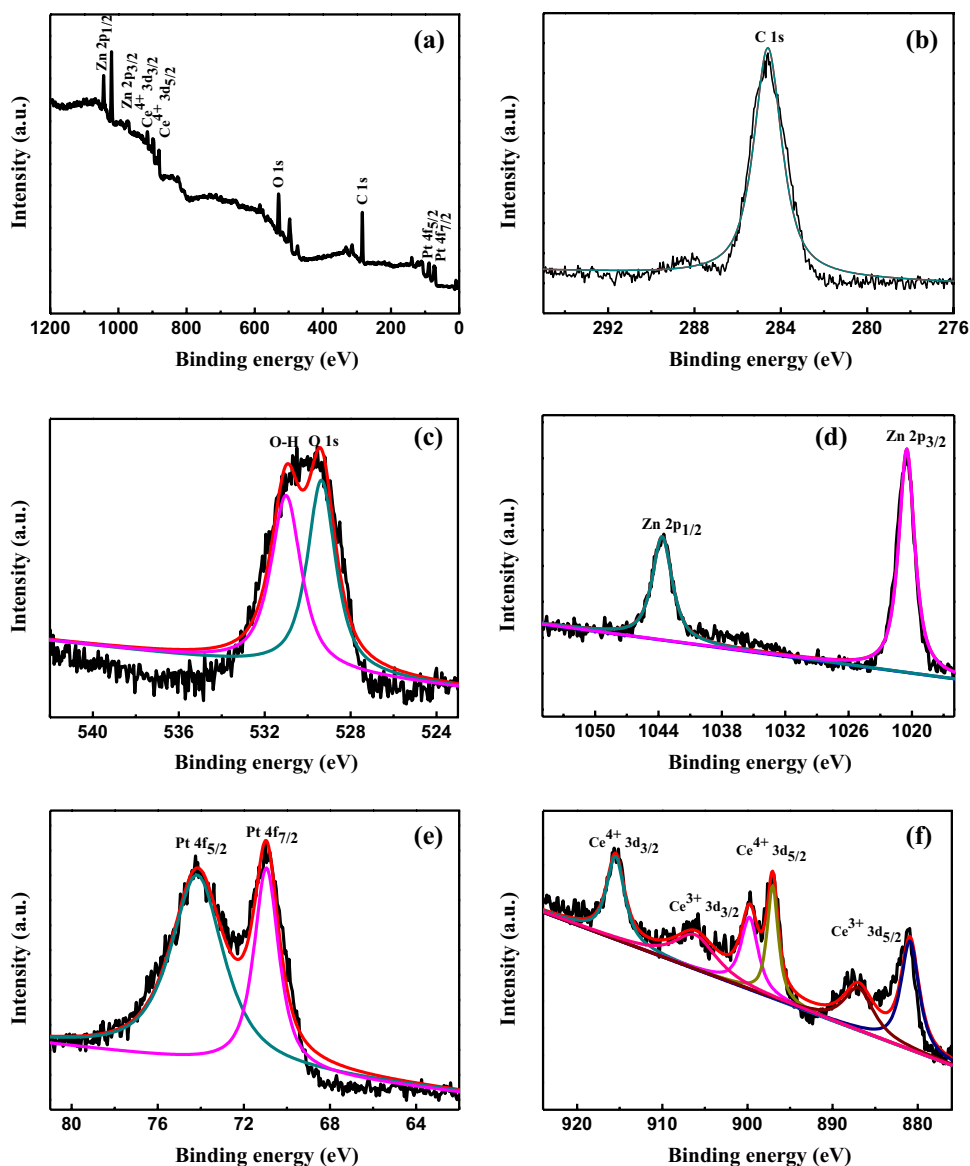
By making a plot of $(\alpha h\nu)^2$ versus $h\nu$, the band gap values for ZnO and CeO₂/ZnO composites are estimated

to ~3.15 eV, and CeO₂ is about 2.98 eV (Fig. 5b). In contrast to other samples, Pt/CeO₂/ZnO composites show additional continuous absorption band in visible light region, which is attributed to the local SPR effect caused by Pt particles (see Fig. 5c).

3.5 SPV and TPV Characterization

SPV and TPV are used to measure the separation efficiency of the photogenerated carriers, which are described in our previous researches [34]. As shown in Fig. 6, both ZnO and CeO₂/ZnO samples show positive SPV signals, indicating that CeO₂ do not change the semiconductor type of the ZnO. However, the SPV signal is negative for pure CeO₂ because of its Ce⁴⁺ ↔ Ce³⁺ redox cycle. Negative SPV signals indicate that photogenerated electrons gather on the surface and photogenerated holes migrate to the bulk phase of the sample. In view of XPS analysis, both Ce³⁺ and Ce⁴⁺ appear on the surface of CeO₂. The Ce⁴⁺ ions can capture electrons and induce electrons move toward the surface, which lead to the negative SPV signals. All of the CeO₂/ZnO composites display the higher SPV signal intensity than that of pure ZnO. On the one hand, the dopant energy level of Ce, acting as the traps to capture the photogenerated electrons, which can improve the efficiency of carriers separation. On the other hand, the CeO₂/ZnO heterojunction is helpful to the transfer of interface charge carriers. Therefore, the synergistic effect of heterojunction and dopant level will contribute to the enhanced separation efficiency of photogenerated charges.

Fig. 4 High-resolution XPS spectra of Pt/3%CeO₂/ZnO catalyst



It is generally known when Pt is loaded on the semiconductor surfaces, it can provide fast transmission channels for electrons so as to reduce the barrier height of semiconductors, which is favorable for the formation of so called ohmic contact at the metal–semiconductor interface. For this reason, we research the change of the photogenerated carriers behavior caused by Pt through TPV testing instrument. The TPV is tested via a 355 nm laser pulse with the intensity of 100 μJ , and the TPV signals are plotted for logarithmic time. As shown in Fig. 7, the signal at the site of 10^{-7} s corresponds to the photovoltage response produced by the drift of photogenerated carriers in the space charge region under the effect of semiconductor self-electric field. The ternary composites exhibit the lower signals intensity, indicates that Pt can weaken the Schottky barrier at semiconductors interface, thus leading to the enhanced photocatalytic activity of

CeO₂/ZnO. The ternary sample exhibits negative signals in the range of 10^{-6} – 10^{-3} s, which indicates photogenerated electrons transfer from CeO₂/ZnO into external Pt NPs after excited by the laser pulse. SPV and TPV test fully prove that Pt/CeO₂/ZnO can provide continuous and fast charges separation and transfer channel, which is propitious to suppress the recombination of the photogenerated electron–hole pairs.

3.6 PL and PA Characterization

PL spectrum is an effective route to investigate the radiative recombination process of the photogenerated electron–hole pairs in the semiconductor. In general, the strong PL intensity means high recombination rate of photogenerated carriers and low photocatalytic activity. From Fig. 8, it is clear that all the samples show the strong main ultraviolet

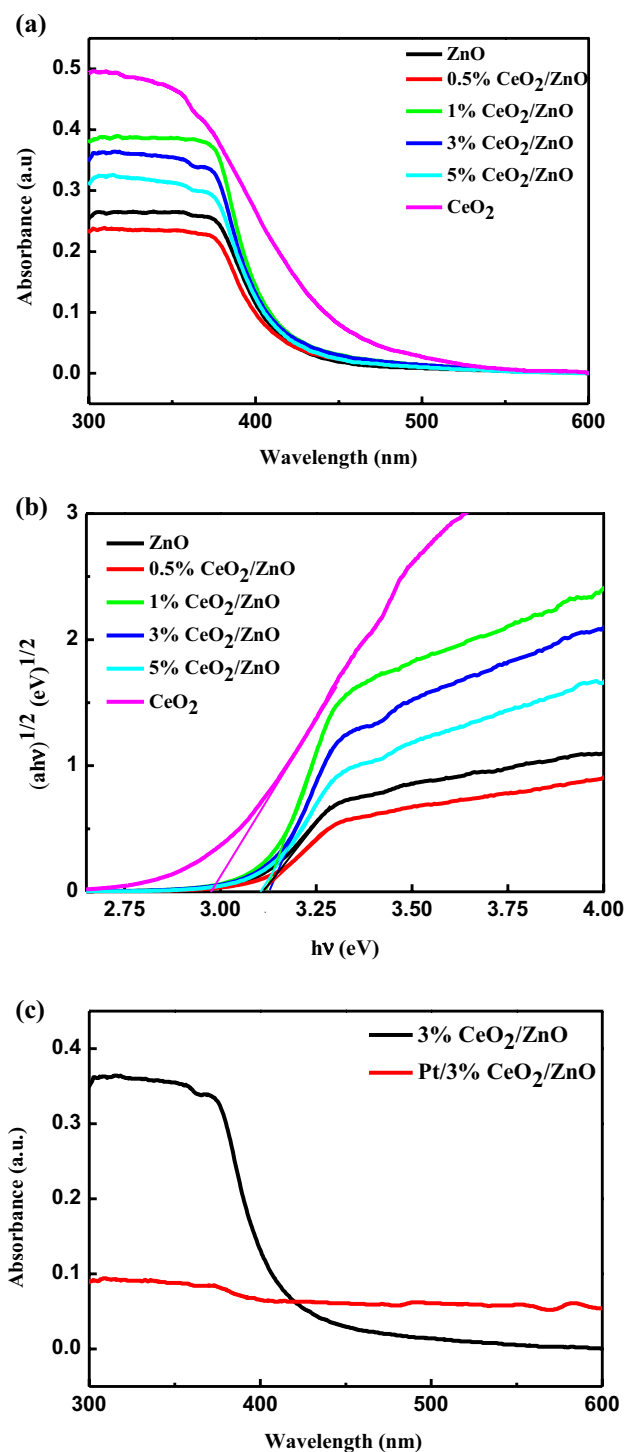


Fig. 5 UV-Vis diffuse reflectance spectra of ZnO, CeO₂, 3% CeO₂/ZnO and Pt/3%CeO₂/ZnO

emission peak located at 400 nm and three weak visible light-emitting bands (blue band at ~447 nm, blue–green band at ~480 nm and green band at ~520 nm). The strong UV emission is related to the near-band-edge transition of photogenerated electron–hole pairs. The blue and green

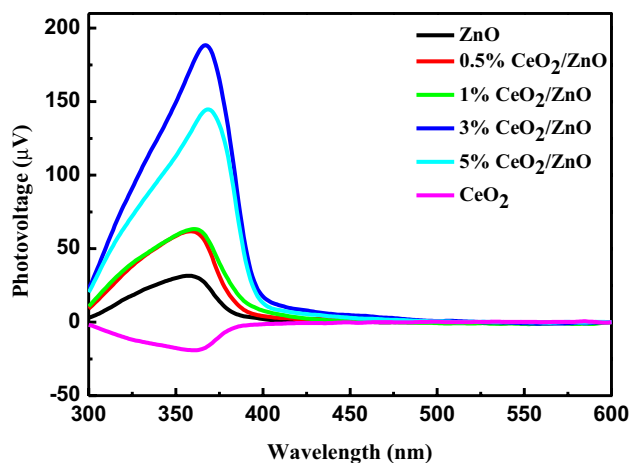


Fig. 6 Surface photovoltage (SPV) spectra of ZnO, CeO₂ and CeO₂/ZnO composites

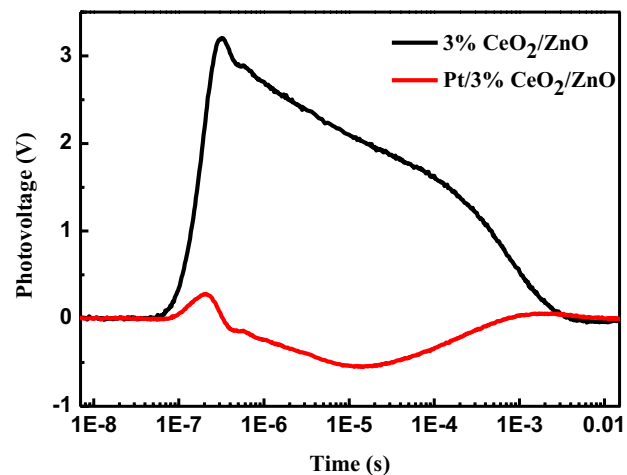


Fig. 7 Transient photovoltage (TPV) spectra of Pt/3%CeO₂/ZnO hybrid

visible light emissions are often associated with deep level defects [35]. As expected, the PL emission intensity of CeO₂/ZnO is dramatically decreased compared with pure ZnO, which means the more effective charge transfer between ZnO and CeO₂. The maximum quenching of PL emission can be found in Pt/CeO₂/ZnO composites. Therefore, we can conclude that this ternary structure is beneficial for the separation of photogenerated electron–hole pairs and reduces radiation transition, which is expected to enhance photocatalytic performance.

PA spectroscopy, as an auxiliary means, is used to study the non-radiative recombination of the photogenerated carriers [36, 37]. In Fig. 9, 3% CeO₂/ZnO sample shows the weaker PA signal intensity than ZnO, which means that the non-radiative recombination is effectively inhibited under the interface electric field between ZnO and CeO₂. However,

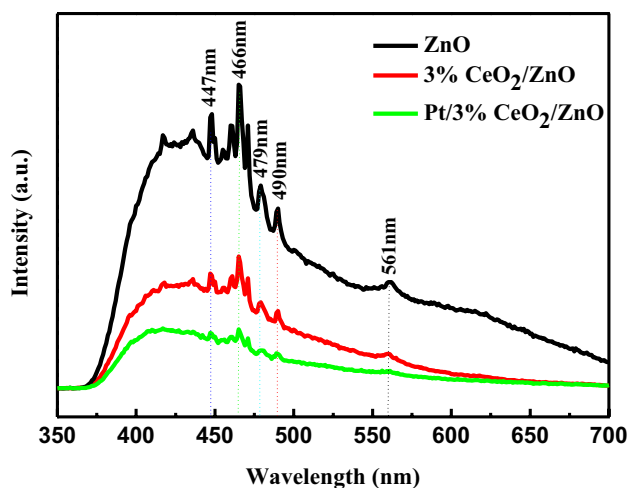


Fig. 8 Room temperature PL spectra of ZnO, 3% CeO₂/ZnO and Pt/3%CeO₂/ZnO with excitation wavelength at 325 nm

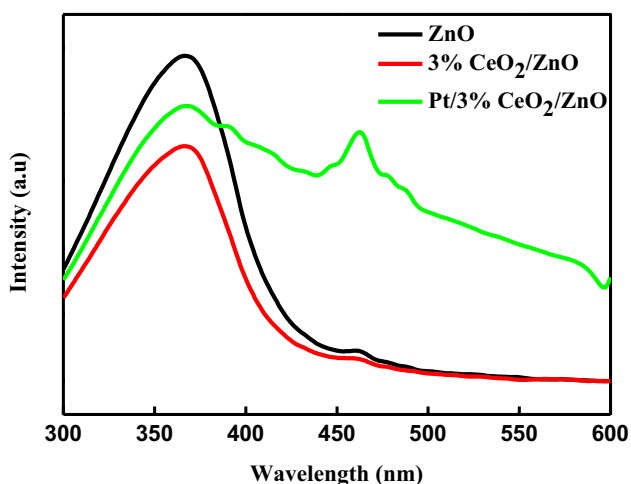


Fig. 9 Photoacoustic spectra of ZnO, 3%CeO₂/ZnO and Pt/3%CeO₂/ZnO composites

the PA response intensity of Pt/CeO₂/ZnO becomes a bit strong. In fact, near the Fermi level of Pt, the energy band change gently meanwhile the width of the energy band is very narrow, so the corresponding density of states is relatively high. The narrower energy band gap indicates the possibility of resonance between two different electronic states, thus makes it easy for non-radiative transition. Therefore, it explains why Pt cannot suppress the non-radiative recombination of photogenerated carriers. In addition, for Pt/CeO₂/ZnO composites, the signal peak around 460 nm originates from SPR effect of Pt. After couple with semiconductor photocatalytic materials, some photogenerated electrons can get out of the bond of Pt atomic nucleus, excited from Fermi level of Pt and transfer to the conduction band of semiconductor. At the same time, strong self building electric field

induces the separation of positive and negative charges in circumferential semiconductors, which improves the photocatalytic properties of the composites.

3.7 Photocatalytic and Stability Test of the Catalyst Test

To study the photocatalytic performance of the prepared products, phenol (25 mg/L) is chosen as a model pollutant. Figure 10 shows the normalized instantaneous concentration change versus time. Pure ZnO and CeO₂ exhibit poor photocatalytic performance and only about 10% phenol can be degraded in an hour. Whereas appropriate amount of CeO₂ will contribute to the improvement of degradation rate, the rise of loaded amount leads to the increase tendency of photocatalytic activities until the content of CeO₂ up to 3%. Also, the photocatalytic activities of 3% CeO₂/ZnO reaches maximum and excessive CeO₂ will become new capture centers of the carriers,

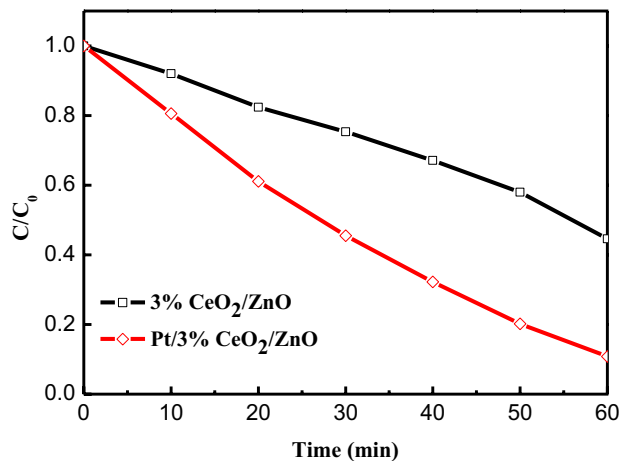
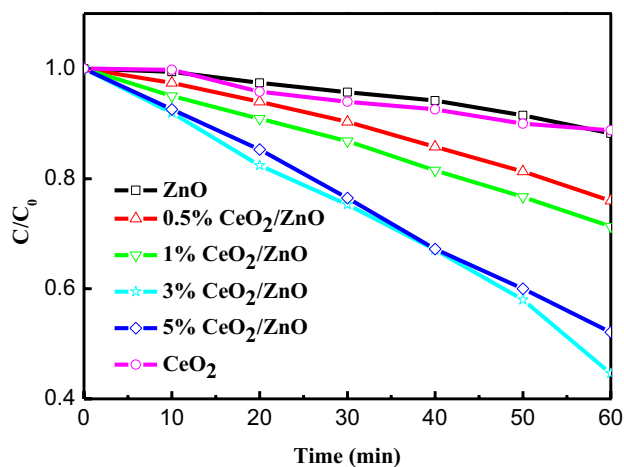
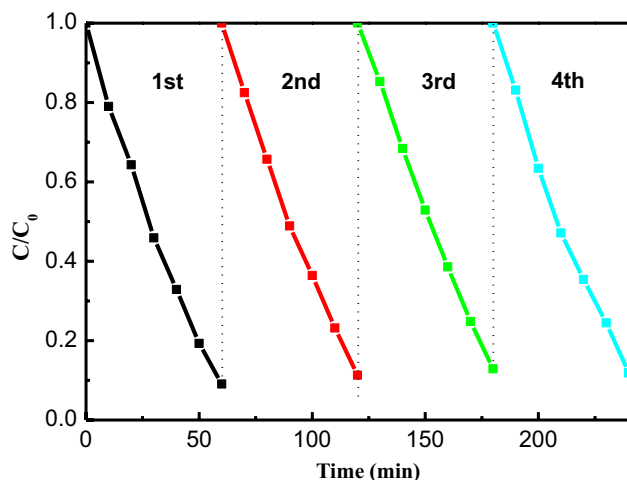


Fig. 10 Time-course variation of C/C_0 of phenol in the presence of different photocatalysts under UV irradiation

Table 1 Comparisons with other related reports from degradation of phenol

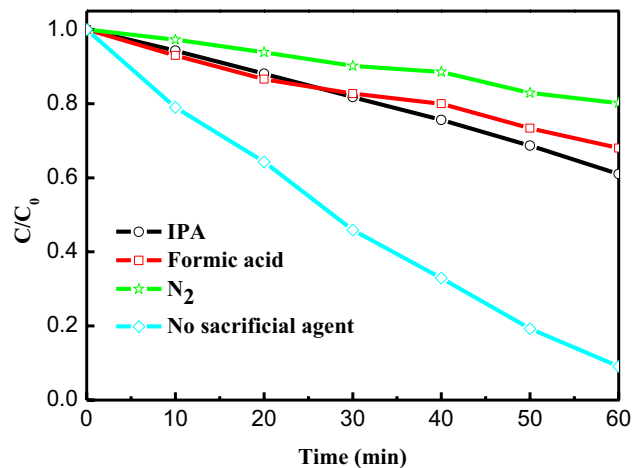
Photocatalyst	Pollutant	Concentration (mg/L)	Light source	Time (min)	Performance
This work	Phenol	25	UV light	60	91%
ZnO [38]	Phenol	20	UV light	300	80.2%
Li/ZnO [39]	Phenol	5	UV–Vis light	120	~ 93.5%
CeO ₂ –TiO ₂ /SiO ₂ [40]	Phenol	30	Visible light	180	96.2%
BiOBr/ZnO [41]	Phenol	10	Sun light	150	98.3%
Pt/ZnO [42]	Phenol	15	UV light	540	Total degradation
C–TiO ₂ –CeO ₂ [43]	Phenol	30	UV light	240	40%

**Fig. 11** Recyclability experiment for photocatalytic degradation of phenol in Pt/3%CeO₂/ZnO system

which brings the slight decay of degradation rate. Moreover, when Pt is attached on the surface of CeO₂/ZnO, the best photocatalytic activity is obtained and phenol removal efficiency reaches 91%.

To intuitively observe the excellent performance of catalyst, we make comparisons with other previous reports and the result is showed in Table 1. The Pt/CeO₂/ZnO composite exhibits superior photocatalytic performance compared to other reports, which is attribute to the strong interaction among the Pt, CeO₂ and ZnO.

For practical application, the cycling test are carried out to make sure the stable photocatalytic activities of Pt/CeO₂/ZnO. After each experiment, the remaining photocatalyst is collected by washed with H₂O and ethanol several times. As shown in Fig. 11, the degradation efficiency of phenol still maintains a high level after four cycles, which proves the as-prepared photocatalyst is quite stable even immerse in phenol solution for a long time. So we can conclude that this novel Pt/CeO₂/ZnO composite has potential application value in the treatment of sewage.

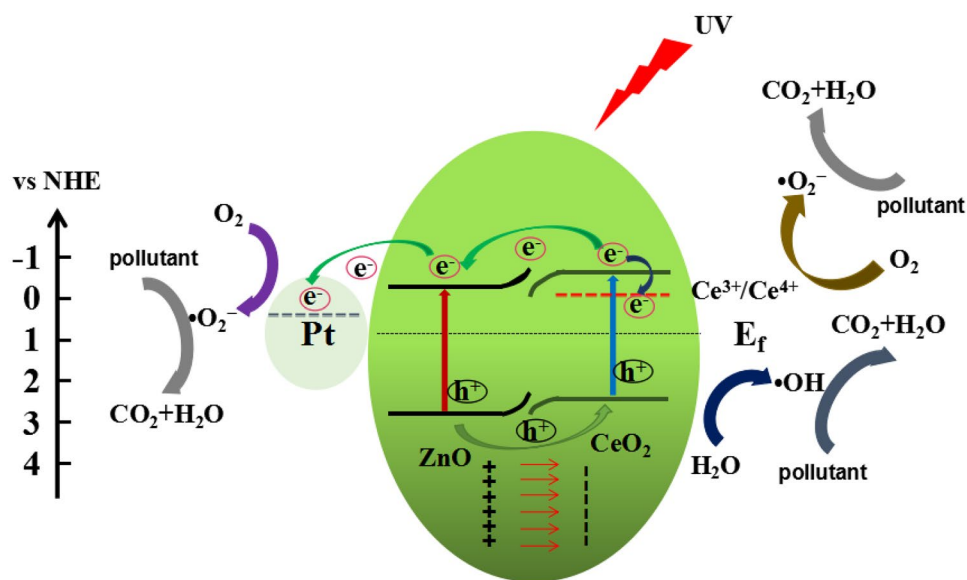
**Fig. 12** Effect of different scavengers on the photodegradation efficiency of phenol under UV light (30 mW/cm²)

3.8 Free Radicals Capture Test and Possible Mechanism of Prepared Samples

Generally speaking, there are three kinds of active substances may take part in the photocatalysis process, hydroxyl radicals ($\cdot\text{OH}$), superoxide anion radicals ($\cdot\text{O}_2^-$) and holes (h^+) [44]. Free radicals capture experiments are carry out to better investigate the reaction mechanism. Formic acid (FA), isopropanol (IPA) and N₂ gas, as the scavengers of h^+ , $\cdot\text{OH}$ and $\cdot\text{O}_2^-$ are put into the photocatalysis reaction system, respectively. As showed in Fig. 12, the degradation efficiency of phenol dropped rapidly with the introduction of IPA and formic acid, but fall most heavily in the sample under N₂ atmosphere. These results show that all the three active substances can take effects in the degradation process, and superoxide anion radicals ($\cdot\text{O}_2^-$) is the dominant one.

Based on the above discussion, the reason for the enhanced photocatalytic activity of Pt/CeO₂/ZnO composites can be attributed to the following two aspects. One is the coexistence of Ce³⁺ and Ce⁴⁺ in the Pt/CeO₂/ZnO composites, the other is suitable energy band location among the ZnO, CeO₂ and Pt materials. Lanthanide ions, acting

Fig. 13 Photocatalytic mechanism of Pt/3%CeO₂/ZnO photocatalytic degradation of phenol under UV light



as Lewis acid, are superior to the oxygen molecule (O₂) in the capability of trapping conduction band (CB) electrons [45]. With the increase of illumination time, Ce³⁺ based CeO_{2-x} defects can be formed via convert CeO₂ to Ce₂O₃. Ce⁴⁺ trap the conduction band electrons of ZnO and form Ce³⁺ (Eqs. 3, 4), the electrons can be further transmitted to the O₂ adsorbed on the ZnO surface and form superoxide anion radicals ·O₂⁻ (Eq. 5) [22]. It is an equilibrium system between Ce³⁺ and Ce⁴⁺ which suppress the recombination of photogenerated electron–hole pairs, and contributed to the formation of superoxide radical anion.



To understand why Pt/CeO₂/ZnO nanocomposites have the higher activity than others, original energy band structures of ZnO and CeO₂ are provided. The location of the conduction band and valence band of semiconductor are determined by the atom's Mulliken electronegativity definition [46]:

$$E_{\text{cb}} = E_{\text{vb}} - E_{\text{g}} \quad (6)$$

$$E_{\text{vb}} = X - E_{\text{e}} + 0.5E_{\text{g}} \quad (7)$$

where *X* is the electronegativity of the semiconductor, which is the geometric mean of the electronegativity of constituent atoms [47]. The *X* values of CeO₂ and ZnO are 5.57 eV and 5.79 eV, respectively; *E_e* is the energy of free electrons on the hydrogen scale (~4.5 eV); *E_g* is the band gap energy of semiconductor (3.15 eV for ZnO, 2.98 eV for CeO₂). The *E_{cb}* and *E_{vb}* of CeO₂ can be calculated to -0.42 eV and 2.56 eV, meanwhile the *E_{cb}* and *E_{vb}* of ZnO are -0.23 eV

and 2.92 eV, respectively. Based on the above data, the theoretical band structure of CeO₂/ZnO n–n heterojunctions can be proposed. When the CeO₂ nanoparticles are coupled on the surface of n-type ZnO, due to the p-type self-doping of Ce³⁺, the Fermi level of CeO₂ is lower than that of ZnO. The electrons will transfer from conduction band of ZnO to the conduction band of CeO₂ until the Fermi levels are equal for both phases, which result in the difference of electrons concentration between the space charge region and bulk phase, thus forming an electron depletion layer and generating an interfacial electric field in where ZnO points to CeO₂. Under UV light irradiation, both ZnO and CeO₂ can be activated and generate electrons and holes. The electrons in conduction band of CeO₂ will transfer to the conduction band of ZnO, the photogenerated electrons will be collected by Pt NPs, and then trapped by O₂ adsorbed on the surface of the ZnO to form ·O₂⁻, ·OH can be generated from the ·O₂⁻ by photochemical reaction, then take part in the photocatalytic process. Simultaneously, the holes in valence band of ZnO will be injected into the valence band of CeO₂. Some of them directly participate in the reaction of mineralizing phenol, another oxidize surface adsorption of OH⁻/H₂O to produce ·OH. In such a way, the non-radiative and radiative recombination of the photogenerated carriers will be suppressed, leading to effective separation of the photogenerated electron–hole pairs and the enhanced photocatalytic activity. Mechanism diagram is depicted in Fig. 13.

4 Conclusions

Ternary composites Pt/CeO₂/ZnO was successfully fabricated through facile hydrothermal and photoreduction method. In this architecture, the existence of the redox cycle

of $Ce^{4+} \leftrightarrow Ce^{3+}$ and the formation of the interface electric field between ZnO and CeO_2 can effectively promote the separation of photogenerated electron–hole pairs. Moreover, Pt acts as acceptor of electrons can provide a fast transmission channel, which is beneficial for the formation of $\cdot O_2^-$. As a result, in contrast to pure ZnO, CeO_2 and CeO_2/ZnO heterojunction, Pt/ CeO_2/ZnO shows superior photocatalytic degradation ability of phenol. More significantly, after four cycles, Pt/ CeO_2/ZnO presents stable photocatalytic activity owing to noble metal maskant. This system provides a new avenue for the purification of wastewater.

Acknowledgements We are grateful to the National Natural Science Foundation of China (Nos. 21872063, 51572106, 21773086).

References

- L. Liu, Y.H. Qi, J.R. Lu, S.L. Lin, W.J. An, Y.H. Liang, W.Q. Cui, *Appl. Catal. B* **183**, 133 (2016)
- J.C. Sin, S.M. Lam, I. Satoshi, K.T. Lee, A.R. Mohamed, *Appl. Catal. B* **148**, 258 (2014)
- J.J. Jiang, P. Zhao, L.Q. Shi, X.Z. Yue, Q.Q. Qiu, T.F. Xie, D.J. Wang, Y.H. Lin, Z. Mu, *J. Colloid Interface Sci.* **518**, 102 (2018)
- V. Etacheri, R. Roshan, V. Kumar, *ACS Appl. Mater. Interfaces* **4**, 2717 (2012)
- D.M. Chen, Z.H. Wang, T.Z. Ren, H. Ding, W.Q. Yao, R.L. Zong, Y.F. Zhu, *J. Phys. Chem. C* **118**, 15300 (2014)
- H.B. Lu, S.M. Wang, L. Zhao, J.C. Li, B.H. Dong, Z.X. Xu, *J. Mater. Chem.* **21**, 4228 (2011)
- Z.Z. Han, L. Liao, Y.T. Wu, H.B. Pan, S.F. Shen, J.Z. Chen, *J. Hazard. Mater.* **217**, 100 (2012)
- C. Tang, L.F. Liu, Y.L. Li, Z.F. Bian, *Appl. Catal. B* **201**, 41 (2017)
- M.X. Sun, Y.Y. Kong, Y.L. Fang, S. Sood, Y. Yao, J.F. Shi, A. Umar, *Dalton Trans.* **46**, 15727 (2017)
- X.J. Lin, M.X. Sun, Y. Yao, X.J. Yuan, *Electrochim. Acta* **291**, 319 (2018)
- Y. Peng, M. Yan, Q.G. Chen, C.M. Fan, H.Y. Zhou, A.W. Xu, *J. Mater. Chem. A* **2**, 8517 (2014)
- Y.J. Wang, R. Shi, J. Lin, Y.F. Zhu, *Energy Environ. Sci.* **4**, 2922 (2011)
- D.G. Wang, P.F. Tan, H. Wang, M. Song, J. Pan, G.C. Kuang, *J. Solid State Chem.* **267**, 22 (2018)
- M.X. Sun, Y.L. Fang, Y.Y. Kong, S.F. Sun, Z.S. Yu, A. Umar, *Dalton Trans.* **45**, 12702 (2016)
- U. Sulaeman, S. Suhendar, H. Diastuti, A. Riapanitra, S. Yin, *Solid State Sci.* **86**, 1 (2018)
- G. Yang, W. Yan, Q. Zhang, S. Shen, S. Ding, *Nanoscale* **5**, 12432 (2013)
- H. Gu, Y. Yang, J.X. Tian, G.Y. Shi, *ACS Appl. Mater. Interfaces* **5**, 6762 (2013)
- J.P. Wang, Z.Y. Wang, B.B. Huang, Y.D. Ma, Y.Y. Liu, X.Y. Qin, X.Y. Zhang, Y. Dai, *ACS Appl. Mater. Interfaces* **4**, 4024 (2012)
- Z.B. Yu, Y.P. Xie, G. Liu, G.Q. Lu, X.L. Ma, H.M. Cheng, *J. Mater. Chem. A* **1**, 2773 (2013)
- M. Nasir, S. Bagwasi, Y.C. Jiao, F. Chen, B.Z. Tian, J.L. Zhang, *Chem. Eng. J.* **236**, 388 (2014)
- C. Wang, H.Q. Fan, X.H. Ren, J.W. Fang, *Appl. Phys. A* **124**, 99 (2018)
- R. Lamba, A. Umar, S.K. Mehta, S.K. Kansal, *J. Alloys Compd.* **620**, 67 (2015)
- Z.L. Yang, J. Lu, W.C. Ye, C.S. Yu, Y.L. Chang, *Appl. Surf. Sci.* **392**, 472 (2017)
- Y.X. Zhu, Z. Chen, T. Gao, Q.L. Huang, F. Niu, L.S. Qin, P. Tang, Y.X. Huang, Z.L. Sha, Y.F. Wang, *Appl. Catal. B* **163**, 16 (2015)
- C.L. Yu, Y. Bai, J.C. Chen, W.Q. Zhou, H.B. He, J.C. Yu, L.H. Zhu, S.S. Xue, *Sep. Purif. Technol.* **154**, 115 (2015)
- H.F. Liang, X.D. Jiang, W. Chen, S.Q. Wang, B.B. Xu, Z.C. Wang, *Ceram. Int.* **40**, 5653 (2014)
- C. Harris, P.V. Kamat, *ACS Nano* **4**, 7321 (2010)
- L.N. Han, D.J. Wang, J.B. Cui, L.P. Chen, T.F. Jiang, Y.H. Lin, *J. Mater. Chem.* **22**, 12915 (2012)
- K.M. Lin, Y.Y. Chen, C.Y. Chiu, *J. Sol–Gel Sci. Technol.* **55**, 299 (2010)
- N. Tian, H.W. Huang, C.Y. Liu, F. Dong, T.R. Zhang, X. Du, S.X. Yu, Y.H. Zhang, *J. Mater. Chem. A* **3**, 17120 (2015)
- T. Montini, M. Melchionna, M. Monai, P. Fornasiero, *Chem. Rev.* **116**, 5987 (2016)
- J.F. Gong, F.M. Meng, X. Yang, Z.H. Fan, H.J. Li, *J. Alloys Compd.* **689**, 606 (2016)
- K. Buvanewari, R. Karthiga, B. Kavitha, M. Rajarajan, A. Suganthi, *Appl. Surf. Sci.* **356**, 333 (2015)
- L.L. Bi, X.P. Gao, L.J. Zhang, D.J. Wang, X.X. Zou, T.F. Xie, *ChemSusChem* **11**, 276 (2018)
- D. Anbuselvan, S. Muthukumar, *Opt. Mater.* **42**, 124 (2015)
- J.J. Jiang, Z. Mu, H.M. Xing, Q.N. Wu, X.Z. Yue, Y.H. Lin, *Appl. Surf. Sci.* **478**, 1037 (2019)
- Y.Y. Lin, K.Y. Li, Q.S. Shan, H. Yin, R.P. Zhu, *Acta Physica Sinica* **65**, 038101 (2016)
- J.C. Sin, S.M. Lam, K.T. Lee, A.R. Mohamed, *Res. Chem. Intermed.* **41**, 2489 (2015)
- N.A. Suhaimi, J.C. Sin, S.M. Lam, A.R. Mohamed, *Mater. Lett.* **154**, 5 (2015)
- C.J. Hao, J. Li, Z.L. Zhang, Y.J. Ji, H.H. Zhan, F.X. Xiao, D. Wang, B. Liu, F.B. Su, *Appl. Surf. Sci.* **331**, 17 (2015)
- F.F. Duo, Y.W. Wang, X.M. Mao, C.M. Fan, H. Zhang, *Cryst. Res. Technol.* **49**, 721 (2014)
- N. Morales-Flores, U. Pal, E.S. Mora, *Appl. Catal. A* **394**, 269 (2011)
- Y. Lara-López, G. García-Rosales, J. Jiménez-Becerril, *J. Rare Earth* **35**, 551 (2017)
- N. Huang, J.X. Shu, Z.H. Wang, M. Chen, C.G. Ren, W. Zhang, *J. Alloys Compd.* **648**, 919 (2015)
- T.Z. Tong, J.L. Zhang, B.Z. Tian, F. Chen, D.N. He, M. Anpo, *J. Colloid Interface Sci.* **315**, 382 (2007)
- S.F. Yang, C.G. Niu, D.W. Huang, H. Zhang, C. Liang, G.M. Zeng, *Environ. Sci.* **4**, 585 (2017)
- X.J. Wang, X.L. Wan, X.N. Xu, X.N. Chen, *Appl. Surf. Sci.* **321**, 10 (2014)

Publisher's Note Springer Nature remains neutral with regard to jurisdictional claims in published maps and institutional affiliations.